Molecular basis of caspase-1 polymerization and its inhibition by a novel capping mechanism

Published in final edited form as:

Nat Struct Mol Biol. 2016 May ; 23(5): 416–425. doi:10.1038/nsmb.3199.

Molecular basis of caspase-1 polymerization and its inhibition by a novel capping mechanism

Alvin Lu[1,2,†], **Yang Li**[1,2,†], **Florian I. Schmidt**[3], **Qian Yin**[1,2], **Shuobing Chen**[4,5], **Tian-Min Fu**[1,2], **Alexander B. Tong**[1,2], **Hidde L. Ploegh**[3,6], **Youdong Mao**[4,5,7], and **Hao Wu**[1,2]

[1]Department of Biological Chemistry and Molecular Pharmacology, Harvard Medical School, Boston, Massachusetts, USA

[2]Program in Cellular and Molecular Medicine, Boston Children's Hospital, Boston, Massachusetts, USA

[3]Whitehead Institute for Biomedical Research, Cambridge, Massachusetts, USA

[4]Center for Quantitative Biology, Peking-Tsinghua Joint Center for Life Sciences, Academy for Advanced Interdisciplinary Studies, State Key Laboratory for Artificial Microstructures and Mesoscopic Physics, School of Physics, Peking University, Beijing, China

[5]Department of Cancer Immunology and Virology, Intel Parallel Computing Center for Structural Biology, Dana-Farber Cancer Institute, Boston, Massachusetts, USA

[6]Department of Biology, Massachusetts Institute of Technology, Cambridge, Massachusetts, USA

[7]Department of Microbiology and Immunobiology, Harvard Medical School, Boston, Massachusetts, USA

Abstract

Inflammasomes are cytosolic caspase-1 activation complexes that sense intrinsic and extrinsic danger signals to trigger inflammatory responses and pyroptotic cell death. Homotypic interactions by Pyrin domains (PYD) and caspase recruitment domains (CARD) in inflammasome component proteins mediate oligomerization into filamentous assemblies. Several cytosolic proteins consisting of only the interaction domains exert inhibitory effects on inflammasome assembly. In this study, we determined the structure of human caspase-1^{CARD} filament by cryo-electron microscopy and investigated the biophysical properties of two caspase-1-like CARD-only proteins,

Correspondence should be addressed to Hao Wu. ; Email: wu@crystal.harvard.edu, 1-617-713-8160

[†]These authors contributed equally to this work

ACCESSION CODES

Caspase-1^{CARD} filament EM map: EMD-3241

Caspase-1^{CARD} structure PDB Code: 5FNA

AUTHOR CONTRIBUTIONS

A. Lu, Y. Li, F. I. Schmidt, Q. Yin, S. Chen, T. Fu, and Y. Mao performed the experiments and analyzed the data. A. Lu, Q. Yin, and T. Fu purified the recombinant proteins and performed biochemical experiments. S. Chen and Y. Mao collected the cryo-EM data, and Y. Li processed the data and completed the helical reconstruction. F. I. Schmidt generated stable cell lines and performed cellular assays, and H. Ploegh supervised the experiments. A. B. Tong performed Rosetta refinement. A. Lu and H. Wu conceived the study and wrote the manuscript.

human inhibitor of CARD (INCA or CARD17) and ICEBERG (or CARD18). Our results reveal the surprising finding that INCA caps caspase-1 filament, thereby exerting potent inhibition with low nanomolar K_i on caspase-1^{CARD} polymerization *in vitro* and inflammasome activation in cells. While caspase-1^{CARD} uses six complementary surfaces of three types for filament assembly, INCA is defective in two of the six interfaces to terminate caspase-1 filament.

As the first line of defense, supramolecular assemblies known as inflammasomes activate inflammatory caspases including caspase-1, caspase-11 (mouse), and caspase-4 and -5 (human) in response to pathogenic invasion and cellular perturbation[1,2]. Absent in melanoma 2 (AIM2)-like receptors (ALRs) and nucleotide-binding domain (NBD) and leucine-rich repeat (LRR) containing proteins (NLRs) are inflammasome sensors and respond to a variety of pathogen-associated molecular patterns (PAMPs) including cytosolic dsDNA and bacterial flagellin, as well as danger-associated molecular patterns (DAMPs) such as extracellular ATP, uric acid crystals, and reactive oxygen species[3]. ALRs and most NLRs contain a Pyrin domain (PYD), which recruits apoptosis-associated speck-like protein containing a CARD (ASC) through PYD-PYD interactions. ASC also possesses a CARD and links the PYD-containing sensor proteins to caspase recruitment, dimerization, and auto-proteolytic activation through CARD-CARD interactions. Both PYD and CARD belong to the death domain (DD) fold superfamily with a conserved six-helical bundle fold[4], and are shown to interact by nucleated polymerization and filament formation[5,6]. The NLR family proteins NLRBs (also known as NAIPs) do not contain a PYD or CARD and signal through the CARD-containing NLRC4 adaptor[7,8], which similarly recruits caspase-1 using CARD-CARD interactions[7,9,10]. Activated caspases proteolytically process pro-interleukin-1β (pro-IL-1β) and pro-interleukin-18 (pro-IL-18). The mature cytokines, once released, can initiate downstream signaling events leading to the transcription of many pro-inflammatory and antiviral genes[11]. Inflammatory caspase activation can also lead to pyroptotic cell death characterized by spillage of cellular contents.

CARD-CARD interactions are essential for the assembly of all inflammasomes. Therefore, it is not surprising that a number of CARD-only proteins (COPs) have been identified to inhibit inflammasome formation and cytokine maturation[12–18]. Regulation by COPs is proposed to arise because of selective pressure and the need for higher tolerance for inflammatory stimuli. Interestingly, rodents and primates all have caspase-1, but COPs are only found in higher primates, which suggests that emergence of these genes must originate after the human/mouse divergence[18]. The genes of proposed CARD-only inhibitors, COP1 (also known as Pseudo-ICE and CARD16), INCA (also known as CARD17), and ICEBERG (also known as CARD18), reside near the caspase-1 locus as a result of a series of gene duplication events[19]. New stop codons led to transcripts missing several downstream exons, resulting in the translation of CARDs lacking the caspase domain[20,21]. INCA and ICEBERG share 83% and 53% identity to caspase-1 CARD respectively, and may have evolved new mechanisms in their functions. Additionally, INCA and caspase-1 are simultaneously upregulated by IFN-γ in human monocytic cell lines THP-1 and U937, and ICEBERG, but not INCA, is induced by LPS and TNF-α[15,16]. Therefore, INCA and ICEBERG may play distinct roles in different biological settings.

To fill the knowledge gap on inflammasome activation and its regulation by CARD-CARD interactions, we determined the caspase-1^{CARD} filament structure using cryo-electron microscopy (cryo-EM), and performed detailed biochemical analyses to understand the mechanisms of inhibition by INCA and ICEBERG. Our results provide the first glimpse of a CARD complex in the pathway and uncover differential functional effects of ICEBERG and INCA. ICEBERG can nucleate caspase-1 filament formation and be incorporated into caspase-1 filaments, but fails to effectively inhibit inflammasome activation. Like previously suggested, ICEBERG may function by interfering with the interaction of caspase-1 with other CARD-containing proteins[17]. In contrast to ICEBERG, we surprisingly reveal that INCA caps caspase-1^{CARD} oligomers to prevent their polymerization, and hence robustly inhibits inflammasome assembly *in vitro* at low nM concentrations. Induced expression of INCA in the THP-1 cell line strongly inhibits inflammasome activation. Collectively, our study expands the structural knowledge on CARD-CARD interactions during inflammasome assembly and regulation.

RESULTS

Cryo-EM reconstruction of the caspase-1^{CARD} filament

We generated a His-MBP-caspase-1^{CARD}-SUMO fusion construct (termed sandwich-tagged) in order to disrupt caspase-1^{CARD} self-oligomerization during over-expression in *E. coli* (Fig. 1a). The fusion protein was purified by size-exclusion as a monomer, and upon removal of the N-terminal His-MBP tag by the Tobacco Etch Virus (TEV) protease, spontaneously formed extended singular filaments in cryo-electron micrographs with a few hundred nanometers in length (Fig. 1b). An average power spectrum revealed visible layer lines that resemble those of the MAVS^{CARD} filament in the RIG-I pathway[22], despite the lack of the meridional layer line (Fig. 1c, Supplementary Fig. 1a). With the assumption of the close similarity, we derived a calculated initial 1-start helical symmetry of −100.23° and 5.06 Å in rotation and rise per subunit respectively (Fig. 1c). Beginning from a solid cylinder model and using iterative helical real-space reconstruction (IHRSR)[23], we obtained a final volume containing mostly α-helices with refined helical parameters of −100.21° and 5.10 Å (Fig. 1d). A homology structure model of caspase-1^{CARD} that we derived from the NMR structure of ICEBERG[16] could be readily positioned into the density, indicating the correctness of the reconstruction (Fig. 1d, Supplementary Fig. 1b–c). The reconstructed volume also displayed disordered density outside the caspase-1^{CARD} filament core, which may correspond to the flexible C-terminal SUMO-tag (Fig. 1d). The reconstruction was estimated to be ~4.8 Å in resolution using both gold standard and model versus map Fourier shell correlation plots, with resolved density for some large side chains (Supplementary Fig. 1b–e), including many at the interface (see below). The final caspase-1^{CARD} model is highly similar to the ICEBERG structure (Supplementary Fig. 1f–g).

Structure of the caspase-1^{CARD} filament

Caspase-1^{CARD} filament has an approximate diameter of 8 nm and an inner hole of < 1 nm (Fig. 2a). Based on an extended conformation of the ~39 residue linker between the CARD and the caspase domain in caspase-1, the closely packed caspase-1^{CARD} in the filament would bring the local concentration of the caspase domain to ~3.1 mM. The caspase-1^{CARD}

filament forms a left-handed 1-start helical assembly consisting of roughly four subunits per turn similar to the Myddosome DD complex and the MAVS^{CARD} filament[22,24], using the previously defined three types of asymmetric interactions[4,25] (Fig. 2b). The type III interface harbors interactions in the helical strand direction. The Type I and type II interfaces provide interaction between the helical turns (Fig. 2c). The type I interface is the most extensive of the three types, with electrostatic complementarity (Fig. 2d). Because of the potential inaccuracies in side chain conformations at this resolution, we describe the type Ia patch as collectively involving residues in helices α1 and α4 (such as K11, R10, R15, R55, and D52), which interact with residues in helix α2 (such as Q31, E28, D27, and N23) (Fig. 2e). In contrast, the type II interaction requires an exposed hydrophobic residue, Y82 in the α5-α6 loop of one subunit, to be inserted into the α2-α3 loop of the adjacent subunit (Fig. 2f). The type III interface appears to be the least extensive and may contribute less binding energy during filament formation (Fig. 2g).

To validate the importance of these interfacial residues, we generated site-directed mutants and compared their properties with wild-type (WT) caspase-1^{CARD} (Fig. 2h–i). We used GFP-tagged caspase-1^{CARD} for these experiments because the fusion protein mostly formed soluble short filaments, similar to the GFP-AIM2^{PYD} protein[26]. We first analyzed whether the mutations reduced the aggregation tendency of GFP-tagged caspase-1^{CARD} using size-exclusion chromatography. We then determined whether the mutations decreased the ability of GFP-tagged caspase-1^{CARD} to promote filament formation of wild-type monomeric caspase-1^{CARD} using fluorescence polarization (FP). For the second experiment, we added a C-terminal sortase motif to the His-MBP-caspase-1^{CARD}-SUMO construct used for cryo-EM. The fusion protein was labeled with the fluorophore TAMRA using recombinant sortase A (Fig. 1a)[27], and caspase-1^{CARD} polymerization was initiated upon removal of the His-MBP tag by the TEV protease. WT GFP-caspase-1^{CARD}, which formed short filaments[5], robustly nucleated caspase-1^{CARD} polymerization, as indicated by increased FP values (Supplementary Fig. 2). The apparent nucleation potency of WT GFP-caspase-1^{CARD} was estimated to be ~283.0 ± 1.4 nM (Supplementary Fig. 2).

While GFP-tagged wild-type caspase-1^{CARD} eluted exclusively at the void volume of a Superdex 200 gel filtration column, charge-reversal mutants of type Ia (R10E K11E) and Ib (D27R E28R) patches abolished caspase-1^{CARD} filament formation, which reflected the importance of electrostatic interactions at the type I interface (Fig. 2h). The Y82E mutant at the type IIb patch also completely abolished filament formation. In contrast, the charge reversal mutant on the type IIa patch, K64E, only impaired, but not abrogated, filament formation, suggesting that the type II interface is likely contributed predominately by hydrophobic interactions. In the caspase-1^{CARD} polymerization assay, K64E was completely incapable of nucleating wild-type caspase-1^{CARD} filament formation (Fig. 2i). Charge reversal mutants at the type IIIa patch (K37E or R45E) did not affect either filament formation or nucleation. Only a more drastic triple mutant (T49R V50R M51R) at the type IIIb surface impaired aggregation and nucleation potency (Fig. 2h–i), consistent with the least extensiveness of type III interactions. These results strongly correlated with our analysis of the caspase-1^{CARD} cryo-EM structure.

Caspase-1^{CARD} filament versus other death domain complexes

We compared the caspase-1^{CARD} filament structure to other existing DD fold complexes by pairwise structural alignment between isolated dimers of caspase-1^{CARD} and dimers of other DD fold complexes. Within the CARD subfamily, MAVS^{CARD} is the only other high-resolution filament structure recently determined by cryo-EM. Despite having very low sequence identity, the helical parameters of MAVS^{CARD} and caspase-1^{CARD} are similar, which might have been determined by the relative location of the interfaces (Supplementary Fig. 3a–c). We also compared the buried residues in respect to each type of interaction, showing that the relative location of these residues indeed correlates very well between the two CARDs (Supplementary Fig. 3d). To have a quantitative comparison, we aligned one subunit of each interface type and measured how much rotation was required to overlap the other subunit (Supplementary Fig. 3e). Between MAVS^{CARD} and caspase-1^{CARD}, rotations for type I, II, and III were 10.2°, 8.1°, and 14.1°, respectively. For comparisons of caspase-1^{CARD} interactions with those of MyD88^{DD} and RAIDD^{DD}, the rotations were respectively 14.1°/8.3°/13.3° and 10.6°/11.3°/21.8°, indicating the more dissimilar quaternary structures. Overall, these angular differences were smaller than the relative rotations between interactions in the caspase-1^{CARD} filament and the ASC^{PYD} filament (14.8°/32.5°/42.3°). This phenomenon may be partially attributed to the helical parameters of the oligomeric structures. Caspase-1^{CARD} filament, MAVS^{CARD} filament, and the Myddosome are all left-handed 1-start helical assembly, while the ASC^{PYD} filament is a right-handed three-start helical assembly[5].

INCA displays distinct properties from caspase-1 and ICEBERG

We expressed His-tagged human INCA and ICEBERG, and found that while INCA was soluble and monomeric, ICEBERG was largely insoluble (Fig. 3a–b). To investigate the biochemical properties of ICEBERG, we fused it to the C-terminus of His-MBP to increase its solubility. His-MBP-ICEBERG was soluble but eluted from the void fraction of a Superdex 200 size-exclusion column. Removal of the His-MBP tag resulted in long and bundled filaments, shown by negative-stain EM (Fig. 3c). The NMR structure of ICEBERG solved at pH 3.8, under which the protein is monomeric[16], shows a typical CARD structure with a six-helix bundle fold that is also highly similar to that of ASC^{CARD} [28]. INCA shares similar predicted secondary structures and 55% sequence identity to ICEBERG with no gaps in the alignment, suggesting that INCA may have a structure highly similar to that of ICEBERG (Fig. 3d). Yet, ICEBERG and INCA have contrasting biophysical properties in solution. Because sequence comparisons revealed identities of 53% for ICEBERG and caspase-1^{CARD}, and 83% for INCA and caspase-1^{CARD} (Fig. 3d), it is therefore the less homologous ICEBERG that shares the filament forming ability of caspase-1^{CARD}, while INCA is monomeric.

ICEBERG promotes and INCA inhibits caspase-1^{CARD} filaments

We employed the caspase-1^{CARD} polymerization assay to probe the effects of the COPs on caspase-1 polymerization. Upon removal of the His-MBP tag by addition of the TEV protease, caspase-1^{CARD}-SUMO formed filaments at a negligibly slow rate as shown by the minimal change in FP (Fig. 4a). ICEBERG greatly enhanced formation of caspase-1^{CARD}

filaments, suggesting that oligomeric ICEBERG provided seeds for polymerization of monomeric caspase-1^{CARD}. In contrast, addition of INCA did not have substantial effects on caspase-1^{CARD} filament formation at its low basal rate.

In ASC-dependent inflammasomes, it is the CARD of the adaptor ASC that nucleates caspase-1^{CARD} polymerization[5]. To recapitulate this *in vitro*, we expressed His-GFP fused to ASC^{CARD}, the majority of which eluted at the void volume of a Superdex 200 size-exclusion column (Fig. 4b). Negative-stain EM indicated that the protein formed short His-GFP-ASC^{CARD} filaments (Fig. 4c). Addition of these ASC^{CARD} filaments at levels well below stoichiometry robustly potentiated caspase-1^{CARD} polymerization, with an apparent dissociation constant (K_{app}) of 108.0 ± 1.4 nM (Fig. 4d). Using fixed His-GFP-ASC^{CARD} and caspase-1^{CARD} concentrations, we added sub-stoichiometric amounts of INCA, and measured the rates of filament formation. Strikingly, very low concentrations of INCA were sufficient to greatly inhibit caspase-1^{CARD} filament formation (Fig. 4e). The apparent inhibitory constant (K_i) was measured at 9.4 ± 1.4 nM (Fig. 4e).

To address the question whether ICEBERG could interact with ASC^{CARD}, we designed an ASC^{CARD} polymerization assay similar to the caspase-1^{CARD} assay. We expressed and purified monomeric His-MBP-ASC^{CARD}-SUMO with a C-terminal sortase motif and labeled the protein with the TAMRA fluorophore *in vitro* using recombinant sortase A. Upon addition of the TEV protease, filamentous His-GFP-ASC^{CARD} acted as a nucleator to polymerize the labeled, His-MBP removed monomeric ASC^{CARD}-SUMO, indicated by increasing FP as a function of time. In contrast, ICEBERG failed to promote ASC^{CARD} filament formation (Supplementary Fig. 4a). Moreover, ICEBERG did not inhibit His-GFP-ASC^{CARD} nucleated ASC^{CARD} polymerization (Supplementary Fig. 4b). Taken together, we conclude that there is no apparent interaction between ICEBERG and ASC^{CARD}.

INCA directly inhibits caspase-1 polymerization

The inhibitory effect of INCA with low nM potency in ASC^{CARD}-induced caspase-1^{CARD} polymerization was remarkable. To determine whether INCA directly interacts with ASC or caspase-1, we co-expressed the proteins in pairs. INCA was cloned into the pDW363 vector with an N-terminally fused biotin acceptor peptide (BAP), which allows biotinylation in *E. coli* by the biotin ligase BirA expressed from the same vector[29]. Biotinylated INCA was first co-expressed with His-GFP-ASC^{CARD}. Ni-NTA affinity purification and gel filtration chromatography yielded strong Coomassie Blue-stained bands of His-GFP-ASC^{CARD}, but no bands of co-purified INCA (Fig. 5a). Streptavidin Western detected a weak band of biotinylated INCA co-purified with His-GFP-ASC^{CARD} (Fig. 5a). To clarify if the apparent weak interaction has any functional importance, we employed the ASC^{CARD} polymerization assay to determine if INCA can inhibit this process. Over-stoichiometric amounts of INCA, at up to 10 μM, did not inhibit His-GFP-ASC^{CARD} nucleated ASC^{CARD} filament formation (Fig. 5b), suggesting that the ASC^{CARD}–INCA interaction does not exert any functional effect.

To determine if INCA interacts with caspase-1^{CARD}, we co-expressed the BAP-INCA fusion with His-GFP-caspase-1^{CARD}. Unlike His-GFP-ASC^{CARD}, His-GFP-caspase-1^{CARD} co-purified with sufficient amounts of INCA to be visible on Coomassie Blue-stained SDS-

PAGE at 7 and 8 ml (Fig. 5c). Streptavidin Western further confirmed that the bands were biotinylated INCA, demonstrating the direct interaction between INCA and caspase-1^{CARD}. CARD domains of both ASC and caspase-1 were present in the assays that we employed to demonstrate inhibition of caspase-1 polymerization by INCA (Fig. 4e). The assay was thus not suitable to determine whether INCA acts on CARD domains of ASC or caspase-1. We therefore performed an alternative experiment using His-GFP-caspase-1^{CARD} as the nucleator. As aforementioned, His-GFP-caspase-1^{CARD} and His-GFP-ASC^{CARD} were similarly potent in nucleating monomeric caspase-1^{CARD} into extended filaments (Fig. 4d, Supplementary Fig. 2). Addition of INCA at very low concentrations dramatically inhibited His-GFP-caspase-1^{CARD} induced caspase-1^{CARD} polymerization (Fig. 5d). The apparent inhibitory constant (K_i) is 4.3 ± 1.4 nM, similar to that obtained in His-GFP-ASC^{CARD} induced caspase-1^{CARD} polymerization (Fig. 4e). We also subjected the His-GFP-caspase-1^{CARD}–biotinylated INCA complex (Fig. 5c) to Streptavidin-gold and Ni-NTA-gold labeling and observed that INCA exclusively localized at the tip of caspase-1^{CARD} filaments (Fig. 5e–f).

The concentrations of monomeric caspase-1^{CARD} and the pre-formed filamentous nucleators used in the polymerization assays were 4.0 μM and 0.1 μM, respectively. The observation that INCA inhibits the polymerization reactions with low nM K_i is intriguing. The inhibitory constant is about three orders of magnitude lower than the concentration of monomeric caspase-1 and about 1/10 to 1/25 of concentrations of the filamentous nucleators. Therefore, a plausible explanation might be that INCA only interacts with the filamentous form of caspase-1. This interaction can directly occur on the His-GFP-caspase-1^{CARD} filaments. When His-GFP-ASC^{CARD} filaments were used, monomeric caspase-1 would polymerize on these nucleators. Then His-GFP-ASC^{CARD}–caspase-1^{CARD} complex filaments became able to directly interact with INCA. It is conceivable that in both cases, the nucleators were capped with INCA, leading to inhibition of polymerization.

Based on the gold labeling experiment (Fig. 5e–f), we quantitatively estimated this strength of inhibition by capping. The average length of the His-GFP-caspase-1^{CARD} filaments was estimated to be ~150 nm based on the electron micrographs. A similar length estimate was derived for His-GFP-ASC^{CARD} filaments (Fig. 4c). Given the observed axial rise per subunit of 5.1 Å for the caspase-1^{CARD} filament, the total number of subunit per filament would be ~30 (Fig. 1d). This suggests that the effective concentration of His-GFP-caspase-1^{CARD} nucleator would be ~30-fold lower, about 3 nM, which brings K_i of INCA inhibition in the same order of magnitude. Collectively, these data are consistent with the conclusion that INCA inhibits caspase-1^{CARD} filament formation by capping small caspase-1^{CARD} containing nucleators.

To test this hypothesis, we performed gel filtration analysis to investigate whether His-MBP-caspase-1^{CARD}-SUMO formed complexes with INCA. At a concentration equivalent to the FP assays, caspase-1^{CARD} was incubated with TEV for 90 minutes at room temperature to remove the N-terminal His-MBP in the presence or absence of slightly over-stoichiometric amount of INCA. As in the experiment shown in Fig. 4a, we expected caspase-1^{CARD}-SUMO to remain mostly monomeric in the absence of a nucleator. Upon completion of the polymerization reaction, the mixtures of MBP-cleaved caspase-1 and INCA were injected to

a Superdex 200 column in order to determine if a stable complex was formed. No apparent shift in the elution position was observed when the two proteins were run individually or as a mixture (Supplementary Fig. 5). This piece of data suggests that INCA does not form a stable complex with caspase-1^{CARD} to sequester the monomeric form, but rather caps the oligomeric form.

ICEBERG interacts with caspase-1^{CARD} filaments by co-mixing

To test whether ICEBERG directly interacts with caspase-1^{CARD}, we used a similar strategy as for INCA and co-expressed biotinylated ICEBERG and His-GFP-caspase-1^{CARD}. Ni-NTA pulldown showed co-purified biotinylated ICEBERG, though sub-stoichiometric to His-GFP-caspase-1^{CARD}, as confirmed by streptavidin Western (Fig. 6a). In size-exclusion chromatography, the complex eluted from the void fraction (Fig. 6b). The complex was then labeled with Ni-NTA-gold and streptavidin-gold conjugates separately and subjected to negative-stain EM analysis to probe the locations of the two proteins in the complex (Fig. 6c–d). The labeling results showed that both gold conjugates randomly labeled the body of the filaments, indicating that ICEBERG co-polymerized with caspase-1^{CARD} into filaments. Therefore, despite the fact that both INCA and ICEBERG have been described as CARD-only proteins, INCA clearly functions through a mechanism different from ICEBERG.

INCA inhibits NLRP3 inflammasome activation in THP-1 cells

Caspase-1 processing and IL-1β secretion are hallmarks of inflammasome activation. We assayed both to monitor the effect of inducible expression of ICEBERG or INCA in THP-1 cells under physiological conditions (Fig. 7). We generated THP-1 cell lines expressing either INCA or ICEBERG. Expression of the transgenes was induced by the addition of doxycycline (D) for 24h before the experiments. Importantly, doxycycline was withdrawn before inflammasome activation because we noticed that expression of any transgene during inflammasome activation impaired IL-1β secretion (data not shown). Cells were then treated for 3h with LPS and for 45 min with nigericin to induce NLRP3 inflammasome assembly. We first analyzed the processing of caspase-1 by an immunoblot, which showed that expression of INCA efficiently inhibited the appearance of the processed forms, while ICEBERG expression had minimal effects (Fig. 7a). Consistently, secretion of IL-1β in wild-type THP-1 cells and un-induced cell lines (-D) was comparable as quantified by ELISA (Fig. 7b). Expression of INCA efficiently inhibited IL-1β secretion in LPS and nigericin-treated cells, while expression of EGFP did not impair IL-1β secretion. Expression of ICEBERG did not have any substantial effect on IL-1β secretion (Fig. 7b).

Therefore consistent with our *in vitro* data, the cellular experiments support a model in which INCA efficiently perturbs caspase-1 cleavage and activity, presumably due the inhibition of caspase-1 polymerization. In contrast, ICEBERG did not seem to inhibit NLRP3-dependent inflammasome activation, caspase-1 oligomerization, and caspase-1 activity. However, the situation in cells is substantially more complex, and it is conceivable that ICEBERG levels are insufficient, or that ICEBERG binding to caspase-1^{CARD} is subject to regulation by cellular proteins. The question whether ICEBERG is, if at all, a genuine inflammasome inhibitor remains to be answered. Even though it physically interacts with caspase-1, the exact molecular mechanism of regulation is unclear.

Structural mechanism of caspase-1 inhibition by INCA

The tendency of death domain fold family proteins to oligomerize into helical oligomers has been shown extensively. Examples of DD helical structures include the PIDDosome (DD)[25], the Myddosome (DD)[24], ASC filament (PYD)[5] and MAVS filament (CARD)[22]. We present the first CARD filament structure in the inflammasome pathway. For INCA to interact with caspase-1, we predict that it must use the similar CARD-CARD interaction surfaces observed in the caspase-1^{CARD} filament structure. By this notion, we superimposed a predicted INCA monomer model based on the NMR structure of ICEBERG onto the caspase-1^{CARD} filament structure, in order to visualize the subtle differences between INCA and caspase-1^{CARD} underlying INCA's inhibitory mechanism (Fig. 8, Supplementary Fig. 6).

For the type I interaction, INCA has a highly similar type Ia interface, marked by the conserved R15 and R55 between caspase-1 and INCA. Strikingly, Asp27 on the caspase-1 type Ib surface is changed to Gly27 in INCA (Fig. 8a). Such change most likely renders the type Ib interface in INCA defective for interaction. According to our mutagenesis studies on caspase-1, type Ib mutation (D27R E28R) completely disrupted filament formation and resulted in the monomeric form of caspase-1 (Fig. 2h). The type II interface is primarily hydrophobic in caspase-1, which relies on Tyr82 for the interaction (Fig. 2f, h). The corresponding position in INCA has changed to His82 (Fig. 8b). This will likely render its type IIb interface defective for interaction. Type III interface represents the least extensive interface and is mostly conserved between INCA and caspase-1^{CARD} (Fig. 8c).

As a result, we propose a model of how INCA inhibits caspase-1^{CARD} via a capping mechanism, based on the defective type Ib and IIb interfaces and the intact type Ia, IIa, IIIa, and IIIb interfaces (Supplementary Fig. 6). During inflammasome activation by filament formation and in the absence of the inhibitory protein INCA, oligomerized ASC^{CARD} domains seed caspase-1^{CARD} filaments (Supplementary Fig. 6a). But in the presence of INCA, a small caspase-1^{CARD} oligomer can stochastically recruit one or a few subunits of INCA through its intact type Ia, IIa, IIIa, and IIIb patches, thereby capping the growing caspase-1 filament. Due to the defective type Ib and IIb patches in INCA, the capped filament then loses the ability to further recruit inactive, monomeric caspase-1 (Supplementary Fig. 6b). This capping mechanism explains the high inhibitory potency of INCA in blocking caspase-1^{CARD} filament formation in our biochemical assay.

In order to test this model, we generated a charge-reversal mutant, R55E, on the type Ia interface of INCA and tested its ability to inhibit GFP-caspase-1 nucleated caspase-1^{CARD} filament formation. Type Ia harbors basic residues that are essential for forming the electrostatic interactions between neighboring CARDs. Therefore, this mutation in INCA is expected to lower its affinity to caspase-1^{CARD} oligomer and thereby abolishes its ability to cap the growing caspase-1^{CARD} filament. Predictably, the R55E mutation substantially reduced the inhibition potency (Supplementary Fig. 7). When we increased the concentrations of R55E in the polymerization assay to drive the inhibition, a K_i of ~1.7 μM for R55E was derived, which is ~400 fold higher than that of wild-type INCA. This piece of data supports our proposed capping mechanism.

DISCUSSION

An emerging theme in the field of innate immunity involves the discovery of higher-order signalosomes in ligand binding and signal transduction[30]. The inflammasome assemblies, in particular, utilize a nucleated polymerization mechanism[5]. Through the formation of filaments and elaborate aggregates in the cell, component proteins come together for efficient activation and signal amplification[5,6]. This mechanism has also been observed in the RIG-I pathway[22,31] and the CARMA1–Bcl10–MALT1 pathway[32], and can be further generalized to related death domain fold containing proteins in other pathways. Extending the initial discovery of INCA as an inhibitor of LPS-induced and caspase-1-dependent IL-1β secretion[1], we investigated its mechanism of inhibition in the context of higher-order inflammasome assemblies. We found that INCA is a strikingly efficient inhibitor of caspase-1^{CARD} oligomerization, with an apparent inhibitory constant in the nanomolar range. We conclude from our biochemical and structural analyses that INCA caps small oligomers of caspase-1^{CARD} through CARD-CARD interactions to prevent the further recruitment of inactive caspase-1 monomers and the elongation of the CARD filaments (Supplementary Fig. 8).

Unlike for INCA, future studies are required to elucidate the functional mechanisms of ICEBERG and COP1. ICEBERG oligomerizes and comingles with caspase-1. COP1 has two isoforms, a short isoform with CARD only and a longer isoform with an additional ~100 residues at the C-terminal end. $COP1^{CARD}$ differs from caspase-1^{CARD} in only three residues, two of which, H15 and Q37, reside at the predicted filamentous interface (Fig. 3d). However, H15 and Q37 are identical in ICEBERG and therefore these differences should not affect the interaction of COP1 with caspase-1. Hence, like ICEBERG, COP1 may also comingle with caspase-1 filaments. It remains to be determined whether ICEBERG and COP1 are bona fide inflammasome inhibitors because our cellular assay failed to show any inhibition of NLRP3 inflammasome activation by ICEBERG.

Numerous studies suggest that inflammasomes may represent important therapeutic targets against human diseases. For example, genetic evidence in the inflammasome sensor proteins NLRP3 (172 known disease variants), Pyrin/MEFV (297 known disease variants), PSTPIP1 (22 known disease variants) and NLRP12 (32 known disease variants) links inflammasomes to hereditary periodic fevers (HPFs), inflammation and autoimmunity. More importantly, over-activation of inflammasomes is causal for or associated with highly prevalent inflammatory diseases within and outside the immune system[1,3,33], including gout, rheumatoid arthritis, dermatitis, lung fibrosis[34], irritable and inflammatory bowel diseases[35], neuropathic pain, sepsis, obesity, atherosclerosis[36], diabetes[37,38], and gastric carcinoma. Many of these diseases have limited treatment options, in particular, those that specifically address the root of the inflammatory response. The capping mechanism by INCA which we discovered here permits interference of inflammasome assembly at a vastly substoichiometric ratio, and provides a new potential therapeutic strategy in inhibition of inflammasomes, as well as the many other innate immune signaling complexes that utilize the death fold domains as the main scaffolding architectures.

Our studies also made a surprising mechanistic connection to capping proteins that dynamically regulate cellular cytoskeletal networks. For instance, the dimeric protein CapZ seals the barbered end of actin filaments to prevent their elongation[39–41]. Human CapZ has an apparent dissociation constant of ~3 nM in actin elongation and depolymerization assays[41]. This is comparable to what we report here for INCA in a caspase-1 polymerization assay. Fungal metabolites known as cytochalasins, which have the ability to bind actin filaments to block their polymerization, offer another example[42]. The effective concentrations of these molecules can range between hundreds of pM to several μM in cells[43]. The apparent equilibrium dissociation constant of cytochalasin D for ADP-actin is ~1–2 nM[44]. Collectively, our studies suggest that INCA may very well be the CapZ or cytochalasin-equivalent inhibitor of caspase-1 filament elongation, and illustrate a potential novel therapeutic mechanism for inflammasome-associated diseases.

ONLINE METHODS

Protein purification

All proteins were expressed in chemically competent BL21(DE3) *Escherichia Coli* cells by overnight induction with 0.4 mM Isopropyl β-D-thiogalactoside (IPTG) at 16 °C. Cells expressing hexahistidine (His)-tagged constructs were lysed by sonication in a buffer containing 20 mM Sodium HEPES at pH 8.0, 150 mM NaCl, 5 mM imidazole, 10% glycerol, and 5 mM β-mercaptoenthanol. Whole cell lysate were centrifuged at 30,000 × g for 40 minutes. The supernatant was incubated with Ni-NTA resin (Qiagen) for 1 hour. The resin was washed with lysis buffer containing 20 mM imidazole. The target proteins were eluted with lysis buffer containing 300 mM imidazole. Subsequent size exclusion purification or gel filtration analysis was done on a Superdex 200 10/300 GL column (GE Healthcare) in a buffer containing 20 mM Sodium HEPES at pH 8.0, 150 mM NaCl, and 2 mM DTT. Biotinylated complexes were expressed and purified using the same procedure except the addition of 50 μM biotin during IPTG induction. The presence of biotin was confirmed by Western blot using streptavidin-conjugated alkaline phosphatase (streptavidine-AP, Molecular Probes Cat# S921).

Cryo-EM data collection

Protein sample (3 μl) was applied to glow discharged holey carbon C-flat grids (R1.2/1.3, Photochip, CA), blotted for 3 seconds, and plunged into liquid ethane in a FEI Vitrobot Mark VI. Frame-packed micrographs were semi-automatically recorded on a FEI Tecnai Arctica Cryo-TEM operating at 200 KeV with a K2 summit direct electron detector, under super-resolution counting mode with 0.87 Å pixel size. A total of 509 video-mode micrographs were collected. The exposure time was 6 seconds and each video stack contained 30 sub-frames, with 200 ms exposure per frame. The accumulated dose in each stack was 20 electron / $Å^2$.

Cryo-EM reconstruction and structure determination

The helical reconstruction was performed using the iterative helical real space reconstruction (IHRSR) method[1]. Each sub-frame was subjected to gain correction and motion correction with SPIDER[2], and then summed up to a single image. Defocus range determined by

CTFFIND3[3] was from 1 to 6 μm. Images with defocus higher than 5 μm or still suffering from severe astigmatism were excluded. 69,222 segments were cut out from the remaining images, with a box size of 200 × 384 pixels and an overlap of 374 pixels (97%). The experimental power spectrum was calculated from the original segments that were padded into 1024×1024 pixels, with a pixel size 0.87 Å. For the diffraction lines marked as n=2, n=−1, n=3 and n=−4, the Y coordinates were measured 78, 49, 29 and 20 pixels respectively, and the X coordinates were approximately 11, −7, 16 and −22 pixels. By indexing the power spectrum, an initial helical symmetry of 5.1 Å in rise and −100.2° in rotation per subunit was obtained. Initial reconstruction was carried on with 4 × 4 binned segments, staring from a solid cylinder to avoid any model bias. Further refinement was gradually expanded to the pixel size of the super-resolution mode. Finally out-of-plane tilt was calculated and imposed to these segments until convergence, leading to the final reconstruction. The final density started to show helical features. To calculate gold standard Fourier shell correlation (FSC)[4], we split sorted dataset into two independent halves. Two parallel helical reconstructions were executed starting from the solid cylinder model and with the same settings and refinement cycles. The resolution was 4.8 Å based on 0.143 cutoff of the gold standard FSC.

Model building and refinement

The nuclear magnetic resonance (NMR) structure of ICEBERG (1DGN)[5] was uploaded to Swiss-Model server[6] to generate an initial caspas-1^{CARD} homology model. The initial model was adjusted manually in COOT[7] toward the cryo-EM density. A filament model containing 8 caspase-1^{CARD} subunits was generated in UCSF Chimera[8] by applying the helical symmetry. The density corresponding to this filament model was masked in CCP4[9] and Fourier transformed to structure factors in the MTZ format using PHENIX[10]. After rigid body phased refinement using PHENIX.refine, the structure was further refined in real space using Rosetta[11]. The model-map cross validation FSC has a value of 0.45 at 4.8 Å resolution.

Sortase labeling and fluorescence polarization assay

Constructs for sortase labeling and polymerization assays contain a C-terminal “LPETG” polypeptide motif. Calcium-independent sortase and TAMRA conjugated tri-glycine nucleophile (GGG-TAMRA) were used[12]. In short, 30 μM of a freshly purified protein substrate with the “LPETG” motif was incubated with 5 μM sortase and 500 μM GGG-TAMRA overnight at 4°C. The labeled substrate and the excess nucleophile were separated by size-exclusion chromatography. Labeled proteins were diluted to desired concentrations for fluorescence polarization (FP) assays on a SpectraMax M5e plate reader. Traces of polarization values were averaged for triplicate experiments and plotted in Excel.

Calculation of apparent dissociation (K_{app}) and inhibitory (K_i) constants

To estimate the apparent dissociation constants between nucleators and polymerizing monomers and the inhibitory constant of INCA, we extracted the slopes of the initial linear phase of the FP traces in the unit of mP/min and plotted them against the log of the concentrations of the added nucleators or INCA. The profiles were fitted in Prism 6.0 for Windows (Graphpad Software, La Jolla California USA, www.graphpad.com) using three-

parameter agonist or antagonist function to determine the concentration of the nucleator or the inhibitor at the half maximal effect.

Nano-gold labeling and negative-stain electron microscopy

Gel filtration purified proteins and protein complexes were embedded on a Formvar carbon-coated EM grid (CFC400-Cu, Electron Microscopy Sciences) and washed 3 times. The grids were blotted to remove excess sample and incubated upside-down on a drop containing suitable dilution of the Ni-NTA gold reagent (5 nm, Nanoprobes, Inc.) or Streptavidin-gold reagent (6 nm, Electron Microscopy Sciences). The grids were washed to remove unbound gold and stained with uranyl acetate for negative-stain EM analysis. More detailed protocols of these experiments can be found in the methods of our previous paper[13].

Generation of INCA and ICEBERG over-expressing THP-1 cell lines

THP-1 human monocyte-like cells (obtained from ATCC) were cultivated in RPMI with 10% FBS and 50 μM 2-mercaptoethanol. THP-1 cell lines inducibly expressing HA-tagged EGFP, ICEBERG, and INCA were generated using lentivirus produced with derivatives of pInducer20[14] and selected in the presence of 500 μg/ml G418. Monoclonal cell lines were obtained by limited dilution in THP-1 medium with 20% FBS. For testing mycoplasma contamination, wild-type and derived THP-1 cells were stained with Hoechst 33342 and analyzed at high magnification. No punctate DNA staining was observed in the cytosol. Alexa Fluor 488 conjugated anti-HA mouse IgG monoclonal antibody (clone 16B12) from Life Technologies (Cat#A21287) was used to confirm HA-ICEBERG and HA-INCA expression in modified THP-1 cells.

NLRP3 inflammasome activation assay

To quantify IL-1β secretion in response to NLRP3 triggers, THP-1 cell lines were seeded into 24-well plates ($2.5{\cdot}10^5$ cells per well) and cultivated in the presence of 50 nM Phorbol-12-myristate-13-acetate (PMA, Santa Cruz Biotechnology) for 16h. Cells were then grown in full medium with or without 1 μg/ml doxycycline for 24h, sensitized in the presence of 200 ng/ml LPS (from *Escherichia coli* K12, InvivoGen) for 3h, and treated with 5 μM nigericin in 0.5 ml OptiMEM per well for 45 min. Control samples were incubated with medium lacking LPS or nigericin, respectively. Supernatants were harvested, cell debris removed by a 10 min spin (1000 × g, 4°C), and samples stored at −20°C. IL-1β levels in a 1:200 dilution of the supernatant were determined using the BD OptEIA Human IL-1β ELISA Set II (BD Biosciences) according to the manufacturer's instructions.

Homology modeling of INCA

A monomeric model of INCA was generated using the online Swiss-Model server[6] with the ICEBERG NMR structure (PDB: 1DGN[5]) as the template. The INCA model was aligned to each subunit of the caspase-1^{CARD} filament cryo-EM structure using the Dali structural alignment server to generate an oligomeric INCA model[15]. Cartoon representations and surface electrostatic potential maps were generated in PyMol (http://www.pymol.org/).

Supplementary Material

Refer to Web version on PubMed Central for supplementary material.

Acknowledgments

The work was supported by the US National Institutes of Health (NIH) grants to H. Wu (Pioneer Award: DP1-HD-087988) and to Q. Yin (R00: 4R00AI108793-02). The cryo-EM facility was funded through the NIH grant AI100645 Center for HIV/AIDS Vaccine Immunology and Immunogen Design (CHAVI-ID). The experiments were performed in part at the Center for Nanoscale Systems at Harvard University, a member of the National Nanotechnology Infrastructure Network (NNIN), which is supported by the US National Science Foundation (NSF) under award no. ECS-0335765. We also thank E. Egelman for his generous guidance on methods of helical reconstruction.

References

1. Lamkanfi M, Dixit VM. Mechanisms and functions of inflammasomes. Cell. 2014; 157:1013–1022. [PubMed: 24855941]
2. Latz E, Xiao TS, Stutz A. Activation and regulation of the inflammasomes. Nat Rev Immunol. 2013; 13:397–411. [PubMed: 23702978]
3. Martinon F, Mayor A, Tschopp J. The inflammasomes: guardians of the body. Annu Rev Immunol. 2009; 27:229–265. [PubMed: 19302040]
4. Ferrao R, Wu H. Helical assembly in the death domain (DD) superfamily. Curr Opin Struct Biol. 2012; 22:241–247. [PubMed: 22429337]
5. Lu A, et al. Unified polymerization mechanism for the assembly of ASC-dependent inflammasomes. Cell. 2014; 156:1193–1206. [PubMed: 24630722]
6. Cai X, et al. Prion-like polymerization underlies signal transduction in antiviral immune defense and inflammasome activation. Cell. 2014; 156:1207–1222. [PubMed: 24630723]
7. Zhang L, et al. Cryo-EM structure of the activated NAIP2-NLRC4 inflammasome reveals nucleated polymerization. Science. 2015
8. Hu Z, et al. Structural and biochemical basis for induced self-propagation of NLRC4. Science. 2015
9. Qu Y, et al. Phosphorylation of NLRC4 is critical for inflammasome activation. Nature. 2012; 490:539–542. [PubMed: 22885697]
10. Kofoed EM, Vance RE. Innate immune recognition of bacterial ligands by NAIPs determines inflammasome specificity. Nature. 2011; 477:592–595. [PubMed: 21874021]
11. Vezzani A, Maroso M, Balosso S, Sanchez MA, Bartfai T. IL-1 receptor/Toll-like receptor signaling in infection, inflammation, stress and neurodegeneration couples hyperexcitability and seizures. Brain Behav Immun. 2011; 25:1281–1289. [PubMed: 21473909]
12. Stehlik C, et al. The PAAD/PYRIN-only protein POP1/ASC2 is a modulator of ASC-mediated nuclear-factor-kappa B and pro-caspase-1 regulation. Biochem J. 2003; 373:101–113. [PubMed: 12656673]
13. Bedoya F, Sandler LL, Harton JA. Pyrin-only protein 2 modulates NF-kappaB and disrupts ASC:CLR interactions. J Immunol. 2007; 178:3837–3845. [PubMed: 17339483]
14. Dorfleutner A, et al. A Shope Fibroma virus PYRIN-only protein modulates the host immune response. Virus Genes. 2007; 35:685–694. [PubMed: 17676277]
15. Lamkanfi M, et al. INCA, a novel human caspase recruitment domain protein that inhibits interleukin-1beta generation. J Biol Chem. 2004; 279:51729–51738. [PubMed: 15383541]
16. Humke EW, Shriver SK, Starovasnik MA, Fairbrother WJ, Dixit VM. ICEBERG: a novel inhibitor of interleukin-1beta generation. Cell. 2000; 103:99–111. [PubMed: 11051551]
17. Druilhe A, Srinivasula SM, Razmara M, Ahmad M, Alnemri ES. Regulation of IL-1beta generation by Pseudo-ICE and ICEBERG, two dominant negative caspase recruitment domain proteins. Cell Death Differ. 2001; 8:649–657. [PubMed: 11536016]
18. Le HT, Harton JA. Pyrin- and CARD-only Proteins as Regulators of NLR Functions. Front Immunol. 2013; 4:275. [PubMed: 24062743]

19. Kersse K, Vanden Berghe T, Lamkanfi M, Vandenabeele P. A phylogenetic and functional overview of inflammatory caspases and caspase-1-related CARD-only proteins. Biochem Soc Trans. 2007; 35:1508–1511. [PubMed: 18031255]
20. Lee SH, Stehlik C, Reed JC. Cop, a caspase recruitment domain-containing protein and inhibitor of caspase-1 activation processing. J Biol Chem. 2001; 276:34495–34500. [PubMed: 11432859]
21. da Cunha JP, Galante PA, de Souza SJ. Different evolutionary strategies for the origin of caspase-1 inhibitors. J Mol Evol. 2008; 66:591–597. [PubMed: 18473111]
22. Wu B, et al. Molecular Imprinting as a Signal-Activation Mechanism of the Viral RNA Sensor RIG-I. Mol Cell. 2014; 55:511–523. [PubMed: 25018021]
23. Egelman EH. The iterative helical real space reconstruction method: surmounting the problems posed by real polymers. J Struct Biol. 2007; 157:83–94. [PubMed: 16919474]
24. Lin SC, Lo YC, Wu H. Helical assembly in the MyD88-IRAK4-IRAK2 complex in TLR/IL-1R signalling. Nature. 2010; 465:885–890. [PubMed: 20485341]
25. Park HH, et al. Death domain assembly mechanism revealed by crystal structure of the oligomeric PIDDosome core complex. Cell. 2007; 128:533–546. [PubMed: 17289572]
26. Lu A, et al. Plasticity in PYD assembly revealed by cryo-EM structure of the PYD filament of AIM2. Cell Discov. 2015; 1
27. Guimaraes CP, et al. Site-specific C-terminal and internal loop labeling of proteins using sortase-mediated reactions. Nat Protoc. 2013; 8:1787–1799. [PubMed: 23989673]
28. de Alba E. Structure and interdomain dynamics of apoptosis-associated speck-like protein containing a CARD (ASC). J Biol Chem. 2009; 284:32932–32941. [PubMed: 19759015]
29. Tsao KL, DeBarbieri B, Michel H, Waugh DS. A versatile plasmid expression vector for the production of biotinylated proteins by site-specific, enzymatic modification in Escherichia coli. Gene. 1996; 169:59–64. [PubMed: 8635750]
30. Wu H. Higher-order assemblies in a new paradigm of signal transduction. Cell. 2013; 153:287–292. [PubMed: 23582320]
31. Hou F, et al. MAVS forms functional prion-like aggregates to activate and propagate antiviral innate immune response. Cell. 2011; 146:448–461. [PubMed: 21782231]
32. Qiao Q, et al. Structural Architecture of the CARMA1/Bcl10/MALT1 Signalosome: Nucleation-Induced Filamentous Assembly. Mol Cell. 2013; 51:766–779. [PubMed: 24074955]
33. Lopez-Castejon G, Pelegrin P. Current status of inflammasome blockers as anti-inflammatory drugs. Expert Opin Investig Drugs. 2012; 21:995–1007.
34. Brusselle GG, Provoost S, Bracke KR, Kuchmiy A, Lamkanfi M. Inflammasomes in respiratory disease: from bench to bedside. Chest. 2014; 145:1121–1133. [PubMed: 24798836]
35. Aguilera M, Darby T, Melgar S. The complex role of inflammasomes in the pathogenesis of Inflammatory Bowel Diseases - Lessons learned from experimental models. Cytokine Growth Factor Rev. 2014; 25:715–730. [PubMed: 24803013]
36. Ridker PM, Luscher TF. Anti-inflammatory therapies for cardiovascular disease. Eur Heart J. 2014; 35:1782–1791. [PubMed: 24864079]
37. Esser N, Legrand-Poels S, Piette J, Scheen AJ, Paquot N. Inflammation as a link between obesity, metabolic syndrome and type 2 diabetes. Diabetes Res Clin Pract. 2014; 105:141–150. [PubMed: 24798950]
38. Robbins GR, Wen H, Ting JP. Inflammasomes and metabolic disorders: old genes in modern diseases. Mol Cell. 2014; 54:297–308. [PubMed: 24766894]
39. Caldwell JE, Heiss SG, Mermall V, Cooper JA. Effects of CapZ, an actin capping protein of muscle, on the polymerization of actin. Biochemistry. 1989; 28:8506–8514. [PubMed: 2557904]
40. Lin YH, Li J, Swanson ER, Russell B. CapZ and actin capping dynamics increase in myocytes after a bout of exercise and abates in hours after stimulation ends. J Appl Physiol (1985). 2013; 114:1603–1609. [PubMed: 23493359]
41. Maun NA, Speicher DW, DiNubile MJ, Southwick FS. Purification and properties of a Ca(2+)-independent barbed-end actin filament capping protein, CapZ, from human polymorphonuclear leukocytes. Biochemistry. 1996; 35:3518–3524. [PubMed: 8639502]

42. Cooper JA. Effects of cytochalasin and phalloidin on actin. J Cell Biol. 1987; 105:1473–1478. [PubMed: 3312229]
43. Wakatsuki T, Schwab B, Thompson NC, Elson EL. Effects of cytochalasin D and latrunculin B on mechanical properties of cells. J Cell Sci. 2001; 114:1025–1036. [PubMed: 11181185]
44. Carlier MF, Criquet P, Pantaloni D, Korn ED. Interaction of cytochalasin D with actin filaments in the presence of ADP and ATP. J Biol Chem. 1986; 261:2041–2050. [PubMed: 3944126]

Method-only references

1. Egelman EH. The iterative helical real space reconstruction method: surmounting the problems posed by real polymers. J Struct Biol. 2007; 157:83–94. [PubMed: 16919474]
2. Shaikh TR, et al. SPIDER image processing for single-particle reconstruction of biological macromolecules from electron micrographs. Nat Protoc. 2008; 3:1941–1974. [PubMed: 19180078]
3. Mindell JA, Grigorieff N. Accurate determination of local defocus and specimen tilt in electron microscopy. J Struct Biol. 2003; 142:334–347. [PubMed: 12781660]
4. Scheres SH, Chen S. Prevention of overfitting in cryo-EM structure determination. Nat Methods. 2012; 9:853–854. [PubMed: 22842542]
5. Humke EW, Shriver SK, Starovasnik MA, Fairbrother WJ, Dixit VM. ICEBERG: a novel inhibitor of interleukin-1beta generation. Cell. 2000; 103:99–111. [PubMed: 11051551]
6. Biasini M, et al. SWISS-MODEL: modelling protein tertiary and quaternary structure using evolutionary information. Nucleic Acids Res. 2014; 42:W252–W258. [PubMed: 24782522]
7. Emsley P, Cowtan K. Coot: model-building tools for molecular graphics. Acta Crystallogr D Biol Crystallogr. 2004; 60:2126–2132. [PubMed: 15572765]
8. Pettersen EF, et al. UCSF Chimera--a visualization system for exploratory research and analysis. J Comput Chem. 2004; 25:1605–1612. [PubMed: 15264254]
9. Winn MD, et al. Overview of the CCP4 suite and current developments. Acta Crystallogr D Biol Crystallogr. 2011; 67:235–242. [PubMed: 21460441]
10. Adams PD, et al. PHENIX: a comprehensive Python-based system for macromolecular structure solution. Acta Crystallogr D Biol Crystallogr. 2010; 66:213–221. [PubMed: 20124702]
11. DiMaio F, et al. Atomic-accuracy models from 4.5-A cryo-electron microscopy data with density-guided iterative local refinement. Nat Methods. 2015; 12:361–365. [PubMed: 25707030]
12. Hirakawa H, Ishikawa S, Nagamune T. Design of Ca2+-independent Staphylococcus aureus sortase A mutants. Biotechnol Bioeng. 2012; 109:2955–2961. [PubMed: 22729808]
13. Lu A, et al. Unified polymerization mechanism for the assembly of ASC-dependent inflammasomes. Cell. 2014; 156:1193–1206. [PubMed: 24630722]
14. Meerbrey KL, et al. The pINDUCER lentiviral toolkit for inducible RNA interference in vitro and in vivo. Proc Natl Acad Sci U S A. 2011; 108:3665–3670. [PubMed: 21307310]
15. Holm L, Sander C. Dali: a network tool for protein structure comparison. Trends Biochem. Sci. 1995; 20:478–480. [PubMed: 8578593]

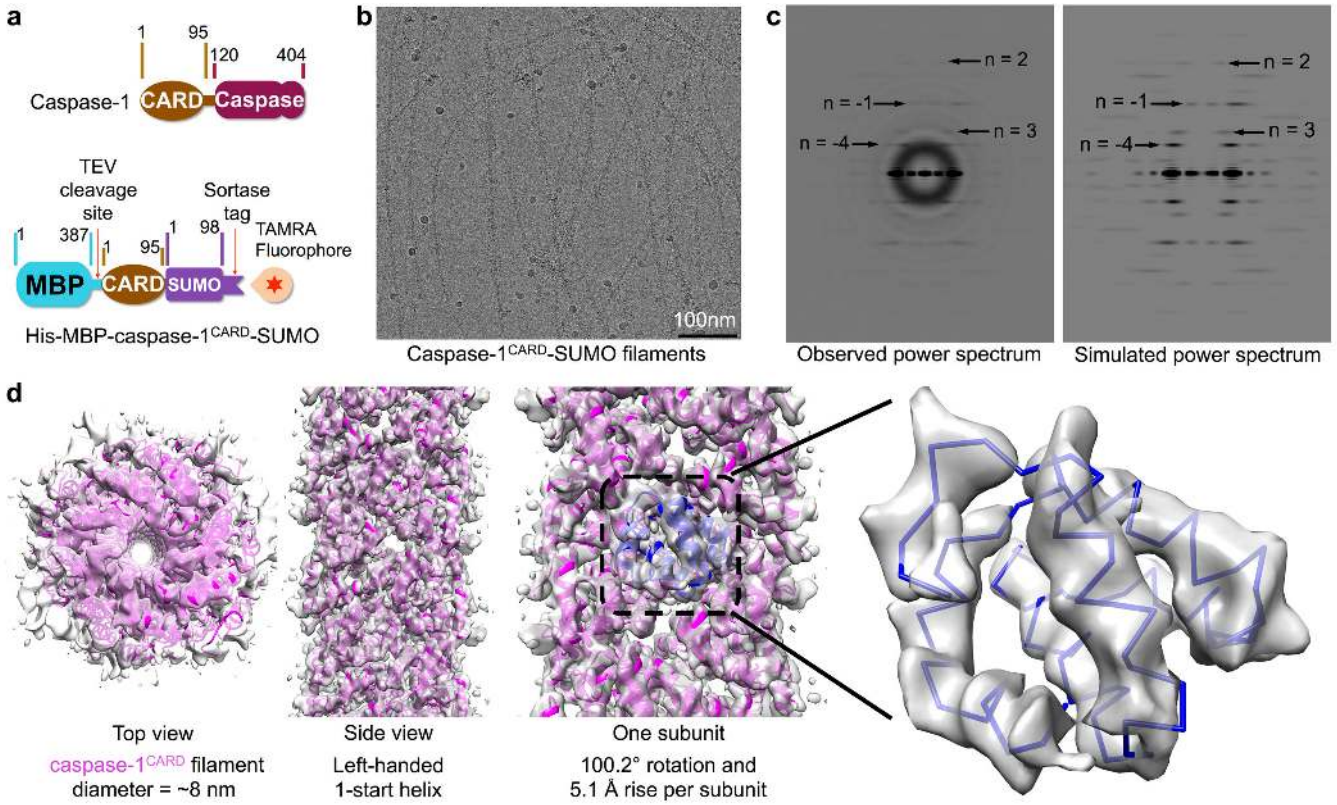

Figure 1.

Cryo-EM structure determination of the caspase-1^{CARD} filament. (**a**) Domain organizations of pro-caspase-1 and its CARD construct for reconstruction and *in vitro* fluorescence polarization assay. (**b**) A representative cryo-EM image. (**c**) Close agreement between experimental and simulated power spectra. Selective layer lines are labeled. (**d**) Reconstructed cryo-EM map fitted with caspase-1^{CARD} model in magenta with one subunit highlighted in blue. At the right, cryo-EM density is shown in zoom and superimposed with a fitted caspase-1^{CARD} molecule.

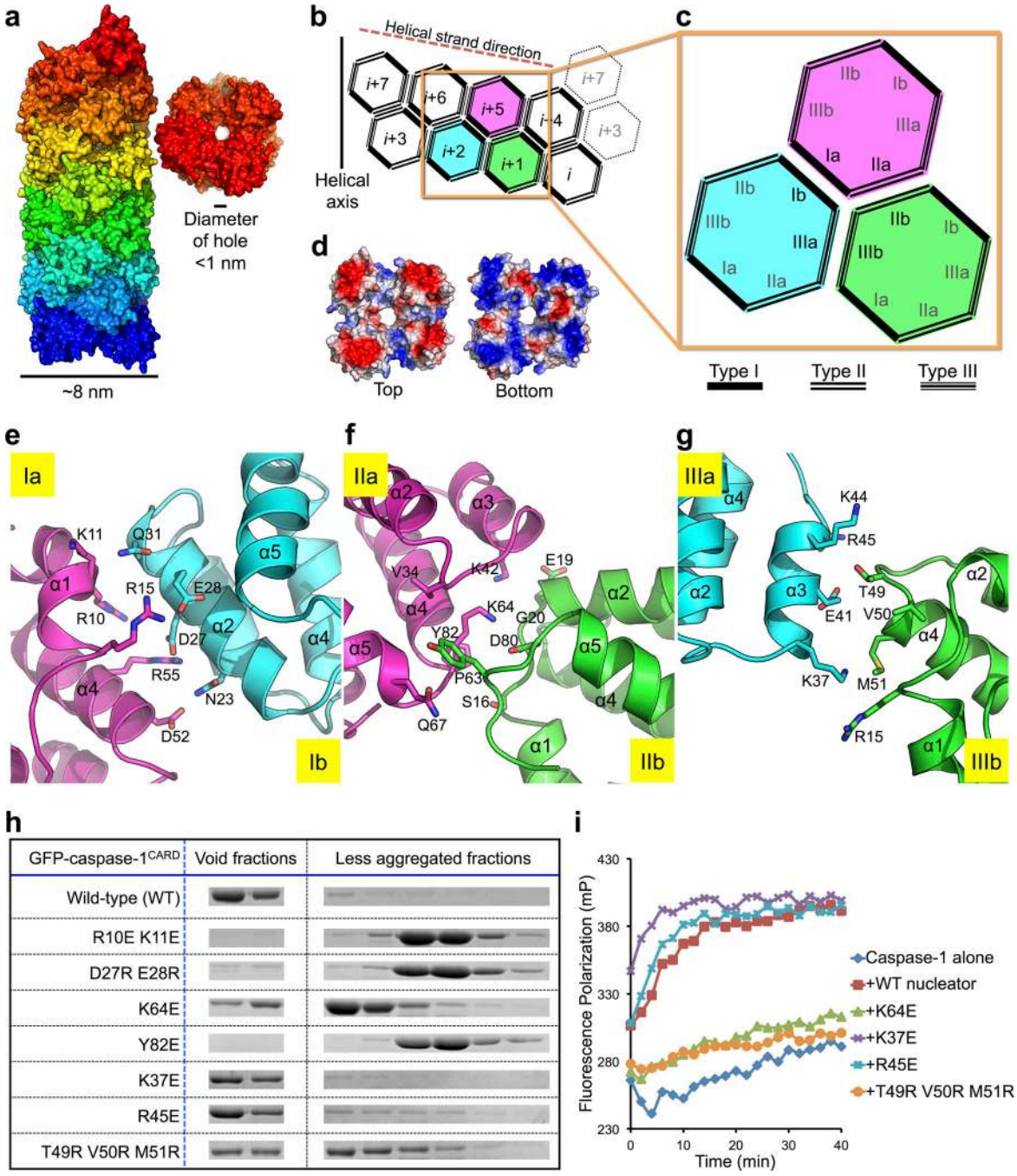

Figure 2.

Structural analysis of the caspase-1^{CARD} filament. (**a**) Surface representation of the caspase-1^{CARD} filament structure. Different subunits are shaded with colors from warm to cold. (**b**) A schematic diagram of the helical filament, with three neighboring subunits highlighted in magenta, green, and cyan. (**c**) Relative orientations of the type Ia, Ib, IIa, IIb, IIIa, and IIIb patches. (**d**) Electrostatic surface renderings of a tetrameric turn showing complementary charges. (**e–g**) The type I (**e**), II (**f**), and III (**g**) interfaces, respectively. Given the current resolution, the precise side chain conformations are not implied in the

representation. (**h**) Size-exclusion chromatography analysis showing void and soluble fractions of wild-type (WT) and mutant capsase-1^{CARD}. Original images of gels can be found in Supplementary Data Set 1. (**i**) Void fractions of wild-type and mutants were further assayed for their potency to nucleate monomeric wild-type caspase-1^{CARD} to form filaments. Approximately 140 nM of each nucleator sample and TEV protease were added to 4 μM of TAMRA-labeled His-MBP-caspase-1^{CARD}-SUMO for polymerization.

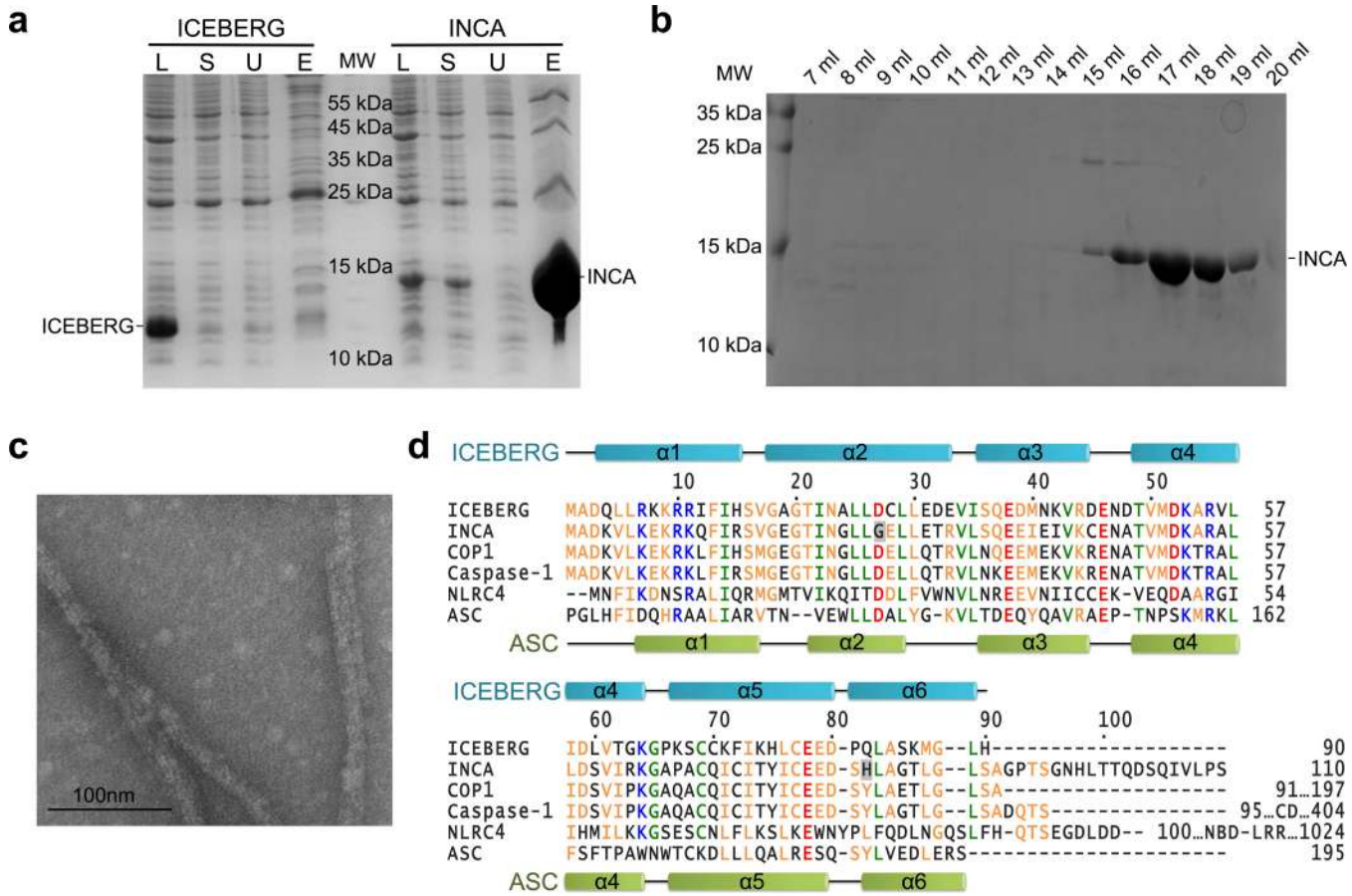

Figure 3.

ICEBERG is filamentous while INCA is monomeric. (**a**) Coomassie Blue-stained SDS-PAGE gel for Ni-NTA affinity purification of *E. coil* expressed 6×His-tagged ICEBERG and INCA. L: whole cell lysate. S: soluble fraction. U: Ni-NTA unbound fraction. E: Ni-NTA elution. ICEBERG appeared as aggregate (at ~12kDa) and INCA (at ~15kDa) could bind to Ni-NTA beads. (**b**) Superdex 200 size exclusion chromatography profile of His-tagged INCA. INCA eluted at monomeric position. (**c**) Negative-stain electron micrograph of MBP-tagged ICEBERG after MBP cleavage. Untagged ICEBERG formed bundled filaments. (**d**) Sequence alignment of ICEBERG, INCA, COP1, ASC^{CARD}, $NLRC4^{CARD}$, and caspase-1^{CARD}. Secondary structures are labeled for ICEBERG and ASC^{CARD}. Regions outside of the aligned CARDs are indicated by residue numbers at the end of the alignment. Caspase-1 has a caspase domain (CD) ending with residue 404. COP-1 has a C-terminal region spanning roughly 100 residues with an unknown fold. NLRC4 has a nucleotide-binding domain (NBD) followed by leucine-rich repeats (LRR) which ends with residue 1024.

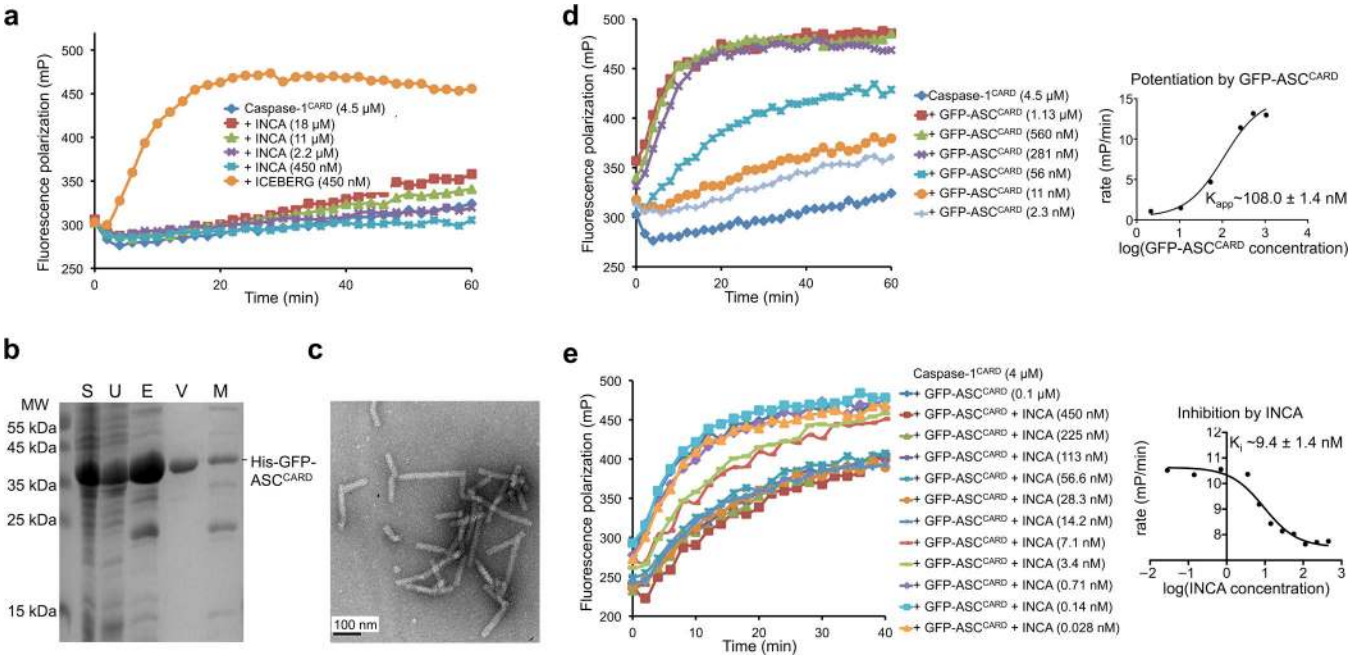

Figure 4.

INCA inhibits ASC^{CARD} nucleated caspase-1^{CARD} filament formation. (**a**) ICEBERG but not INCA nucleated caspase-1^{CARD} filament formation. Average of triplicate experiments were plotted. (**b**) Ni-NTA affinity purification and size exclusion chromatography of His-GFP-tagged ASC^{CARD}. S: soluble fraction of bacterial lysate. U: Ni-NTA unbound fraction. E: Ni-NTA elution. V: void fraction on gel filtration. M: monomer fraction on gel filtration. (**c**) Negative-stain electron micrograph of the His-GFP-ASC^{CARD} void fraction. Scale bar at 100 nm. (**d**) Nucleation effect of GFP-tagged ASC^{CARD} at different concentrations on caspase-1^{CARD} filament polymerization. Calculation of the apparent dissociation constant (K_{app}) is shown on the right. (**e**) Inhibitory effect of INCA at different concentrations on His-GFP-ASC^{CARD} nucleated caspase-1^{CARD} filament formation. Calculation of the apparent inhibitory constant (K_i) is shown on the right.

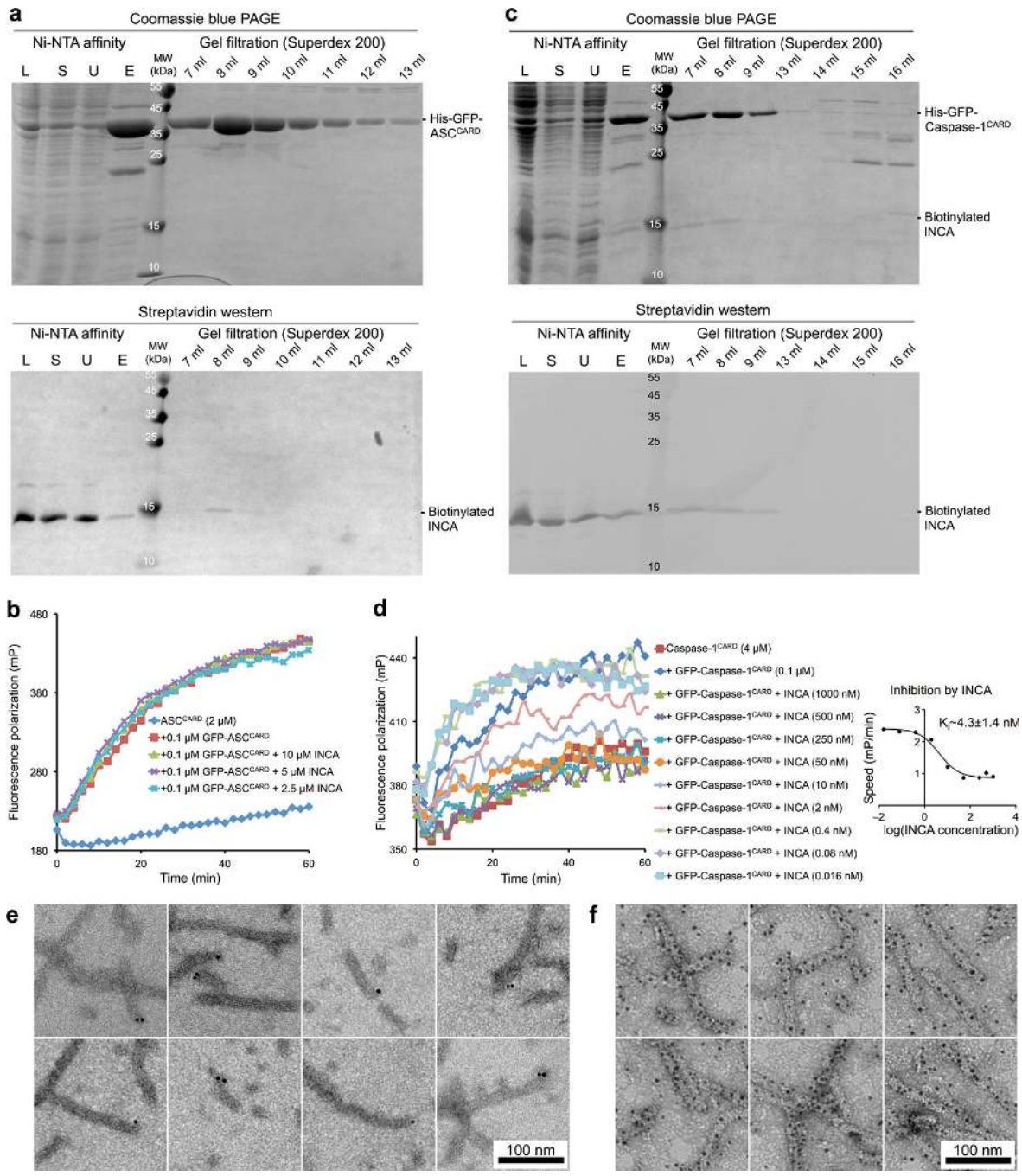

Figure 5.

INCA preferentially interacts with caspase-1^{CARD}. (**a**) Co-expression of His-GFP-ASC^{CARD} and biotinylated INCA showed no significant interaction between INCA and ASC^{CARD}, as indicated by the Western blot. (**b**) Over-stoichiometric amounts of INCA did not inhibit His-GFP-ASC^{CARD} nucleated ASC^{CARD} filament formation. Averages of triplicate experiments were plotted. (**c**) Co-expression of His-GFP-caspase-1^{CARD} and biotinylated INCA showed interaction between INCA and caspase-1^{CARD}, as confirmed by the PAGE gel. (**d**) Sub-stoichiometric amounts of INCA inhibited His-GFP-caspase-1^{CARD} nucleated

caspase-1^{CARD} filament formation. Averages of duplicate experiments were plotted. (**e–f**) Negative-stain electron micrographs of the complex (as shown in panel **c** at 7 ml) between His-GFP-caspase-1^{CARD} and biotinylated INCA after streptavidin-gold labeling (**e**) or Ni-NTA-gold labeling (**f**).

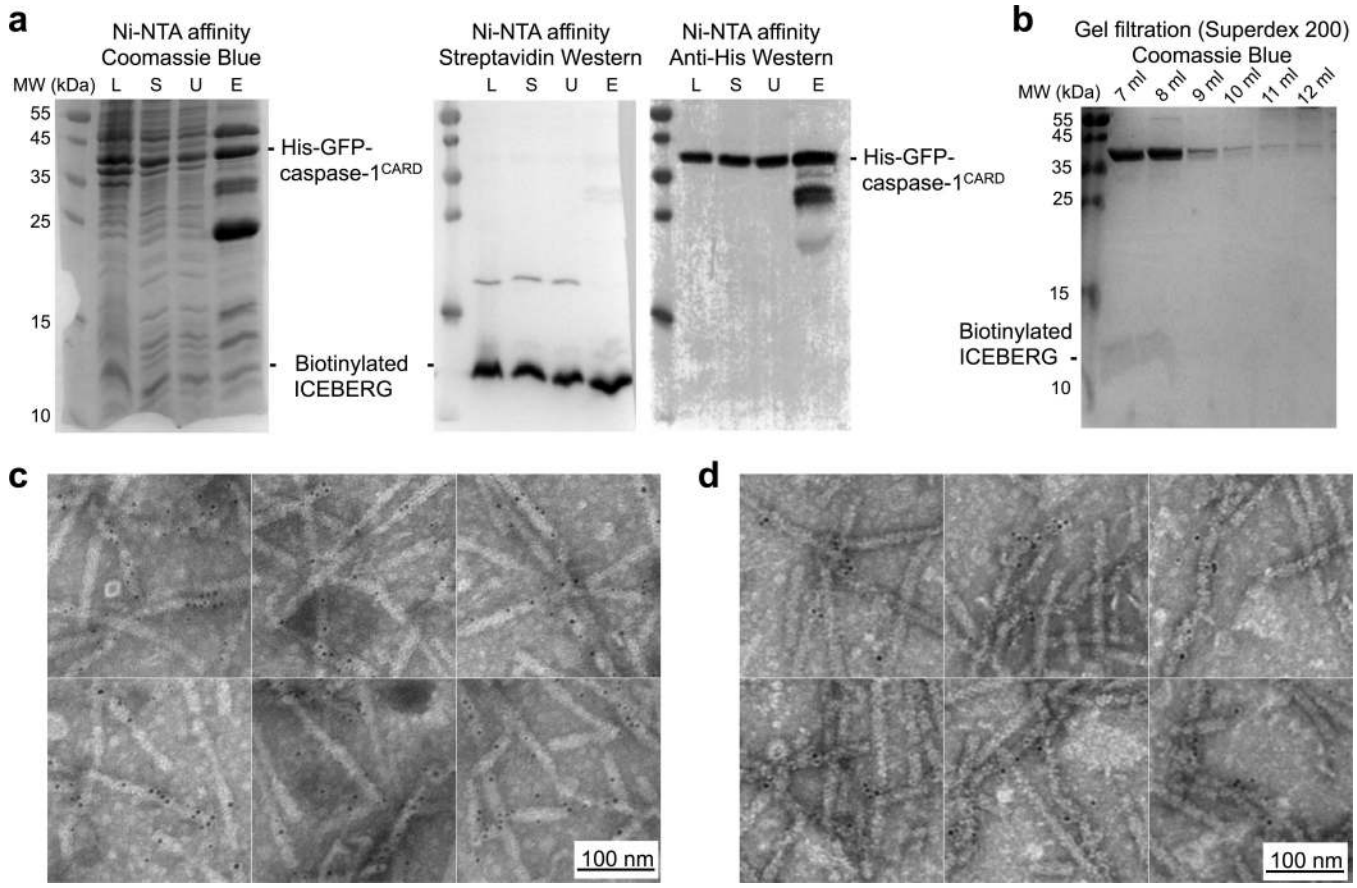

Figure 6.

ICEBERG interacts with caspase-1^{CARD} by co-mixing. (**a**) Co-expression of His-GFP-caspase-1^{CARD} and biotinylated ICEBERG. Streptavidin-AP and anti-6×His-tag Western blots were shown to confirm the presence of ICEBERG in complex with His-GFP-caspase-1^{CARD} after Ni-NTA affinity chromatography. L: Whole cell lysate. S: Soluble fraction. U: Ni-NTA unbound. E: Ni-NTA elute. (**b**) The complex eluted from the void of a Superdex 200 column. (**c–d**) Negative-stain electron micrographs of the complex (as shown in panel **b** at 7 ml) between His-GFP-caspase-1^{CARD} and biotinylated ICEBERG after Ni-NTA-gold labeling (**c**) or streptavidin-gold labeling (**d**).

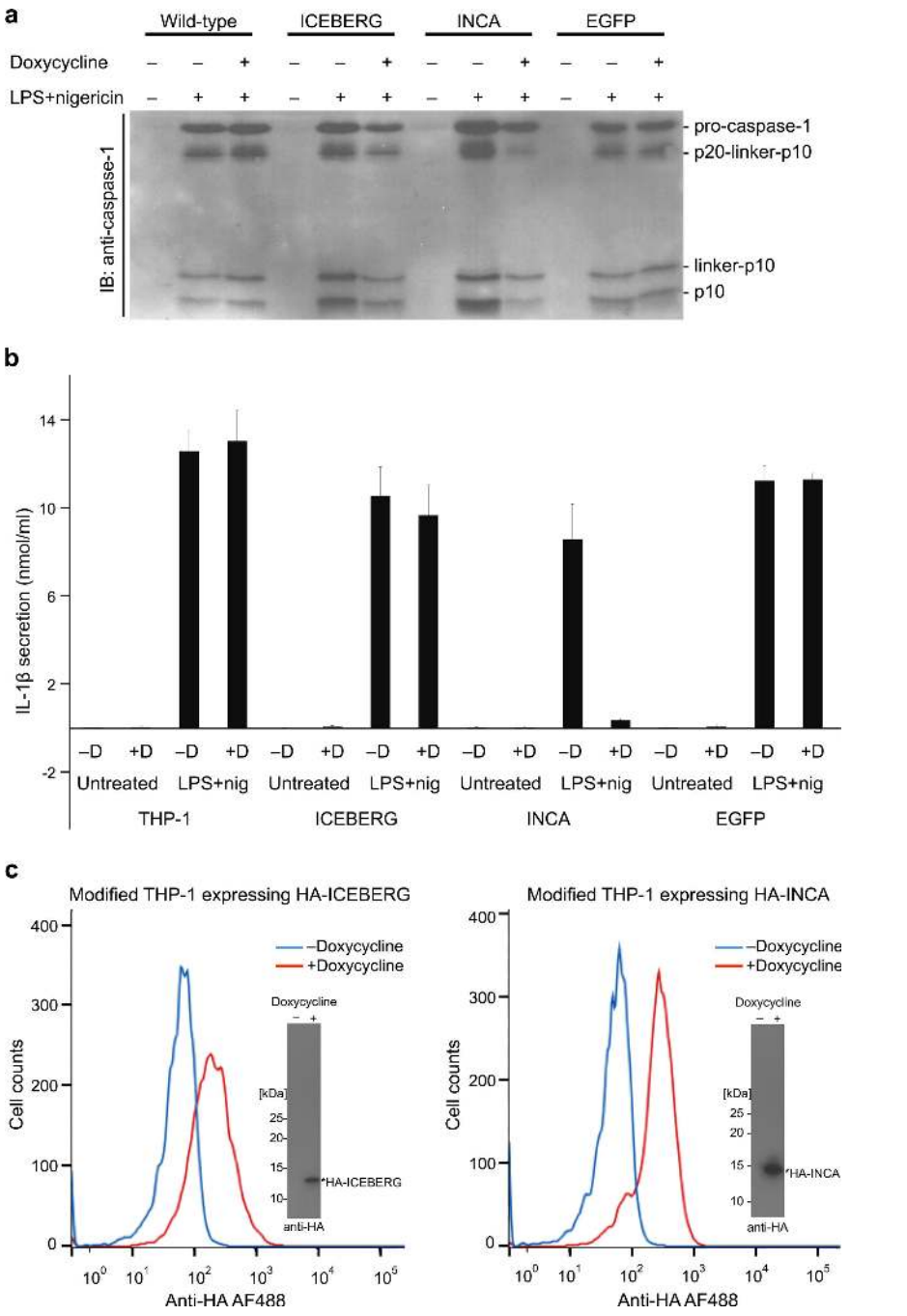

Figure 7.

Inducible expression of ICEBERG and INCA on NLRP3 inflammasome activation in modified THP-1 cells treated by LPS and nigericin (Nig). (**a**) Caspase-1 processing in wild-type (WT) (unmodified THP-1) and modified THP-1 cells carrying the ICEBERG or INCA transgene. (**b**) ELISA assay for IL-1β secretion for unmodified and modified THP-1 cells carrying ICEBERG or INCA transgenes. Doxycycline (D) served to induce the expression of transgene. THP-1 cells carrying the EGFP transgene were used as a control. Averaged results ± s.e.m. are shown for 3 independent experiments of inflammasome stimulation in

the wild-type or stable cell lines. (**b**) Control experiment showing the inducible expression of HA-ICEBERG and HA-INCA in modified THP-1 cell lines as detected by Alexa Fluor 488 conjugated anti-HA antibody.

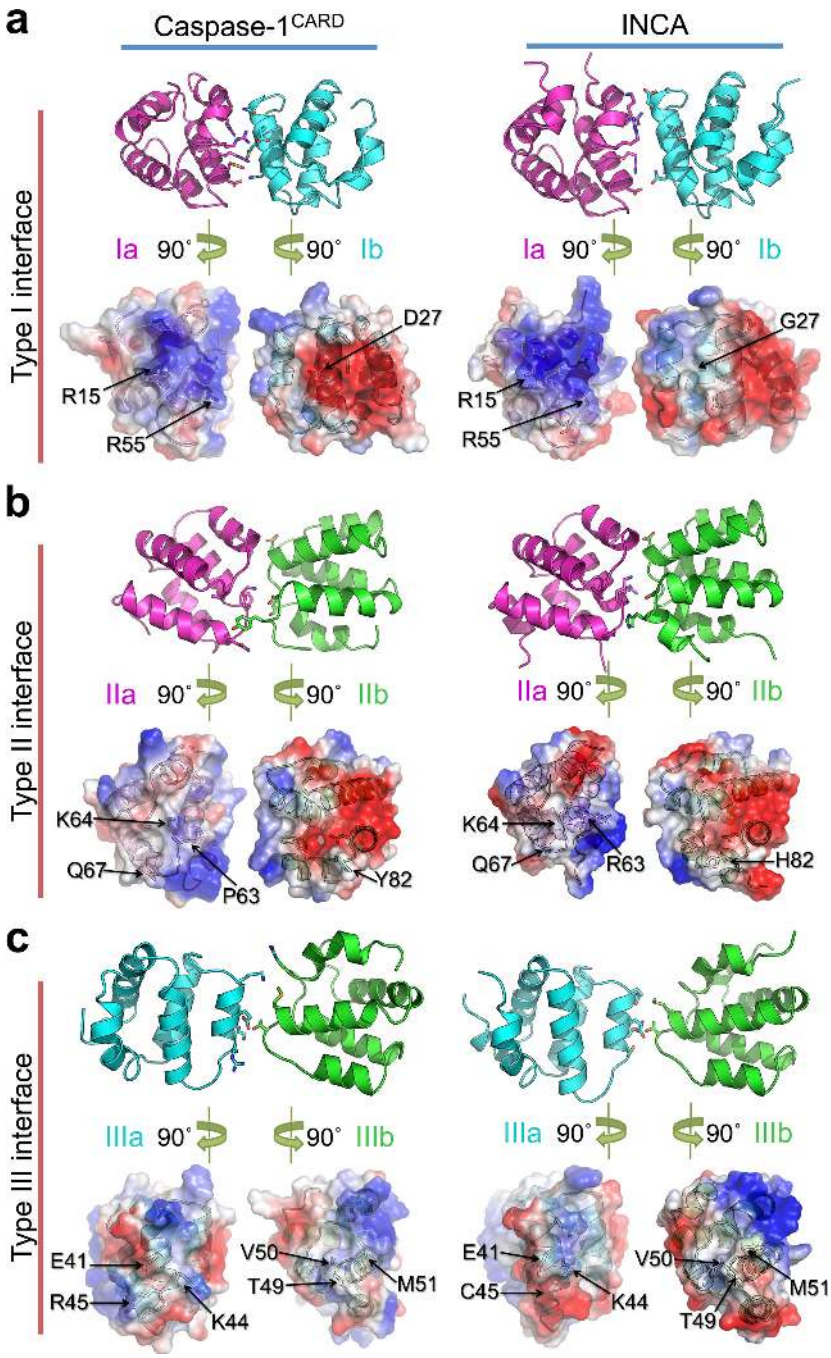

Figure 8.

Comparison of critical interfacial residues between caspase-1^{CARD} and INCA. Model of an INCA monomer was generated using ICEBERG NMR structure as template (PDB: 1DGN). It was superimposed on each of the subunit in the caspase-1^{CARD} filament cryo-EM structure using the Dali pairwise structural alignment online server. Type I, II, and III interfaces of caspase-1^{CARD} and INCA are compared side by side, as shown in (**a**), (**b**), and (**c**) respectively. Each of the colors (magenta, cyan, or green) indicates the same subunit

across the three interface types. Electrostatic surface representations of the interfaces are marked with critical residues for comparison.